Chinese Journal of Structural Chemistry 45 (2026) 100767

Contents lists available at ScienceDirect

Chinese Journal of Structural Chemistry

journal homepage: www.journals.elsevier.com/chinese-journal-of-structural-chemistry

Article

One-dimensional $(C_{12}H_{12}N)_3Cu_3I_6$ for high-performance direct X-ray detection

Pan Gao[a], Qingzheng Kong[a], Ying Sun[a], Qian Ma[b], Qi Wang[a], Zeyu Guo[a], Ledi Li[a], Bingbing Li[a], Jingwei Xu[a], Xiaomei Jiang[a,*], Zhaolai Chen[c]

[a] *School of Preventive Medicine Sciences (Institute of Radiation Medicine), Shandong First Medical University & Shandong Academy of Medical Sciences, Jinan, 250117, China*

[b] *School of Material Science and Engineering, University of Jinan, Jinan, 250022, China*

[c] *State Key Laboratory of Crystal Materials (Institute of Crystal Materials), Shandong University, Jinan, 250100, China*

A R T I C L E I N F O

Keywords:
Organic copper halides
One-dimensional structure
X-ray detection
X-ray imaging

A B S T R A C T

X-ray detectors, as crucial elements in medical imaging and industrial fields, can be categorized into direct and indirect types. Direct detectors, which directly convert X-ray photons into electrical signals, exhibit high sensitivity and low detection limits, enabling the capture of high-resolution images and reducing radiation exposure to patients. Organic copper halides, recognized as potential active materials for X-ray detection, have been widely explored in the indirect scintillation field but remain under-explored in direct X-ray detector applications. In this work, $(C_{12}H_{12}N)_3Cu_3I_6$ is demonstrated as an efficient semiconductor for direct X-ray detection with excellent stability. A lateral-structured X-ray detector was fabricated with gold electrodes, which exhibits a maximum sensitivity of 1464.14 $\mu C \cdot Gy^{-1} \cdot cm^{-2}$, a lowest detection limit of 19.8 $nGy \cdot s^{-1}$, a high on-off ratio of 2140, and an excellent operational stability of retaining 96% performance after 600 s continuous X-ray radiation. Furthermore, the detector successfully imaged a 0.1 mm “F”-shaped lead sheet, validating its capacity for X-ray imaging. This study highlights the potential of $(C_{12}H_{12}N)_3Cu_3I_6$ as a promising semiconductor for high-performance direct X-ray detection, expanding the application scope of organic copper halides in this critical field.

1. Introduction

Direct X-ray detectors are typically composed of semiconductor materials, which enable the direct conversion of X-ray photons into electrical signals [1–6]. These detectors with high sensitivity and low detection limit play a pivotal role in minimizing the radiation dosage administered to patients during X-ray imaging procedures. This feature is of profound significance for mitigating cancer risks while facilitating the acquisition of high-resolution images, thereby enhancing diagnostic accuracy [7–11]. Currently, traditional semiconductor materials commonly used for X-ray detectors, such as α-Se and CdTe, still suffer from limitations including low absorption efficiency for high-energy X-rays as well as complex and expensive manufacturing processes [12–17]. Comparatively, lead halide perovskites have emerged as a viable alternative, attributed to their facile solution-processable growth and superior performance [18–20]. Despite their exceptional potential in this field, the inherent lead toxicity has posed great environmental risks, thereby driving the urgent search for environmentally sustainable alternatives [21,22]. In recent years, the emergence of lead-free organic metal halides (OMHs) has sparked a new research frontier [23–25]. Among the emerging candidates, Cu-based OMHs have garnered significant attention due to their cost-effective and widely available raw materials, low toxicity, and tunable optoelectronic properties [26]. Most reported copper(I)-based OMHs to date are characterized by zero-dimensional (0D) structure, featuring isolated Cu–I units without continuous lattice connections, such as 0D $(ETPP)_2Cu_2I_4$ [27], 0D $(18\text{-crown-6})_2Na_2(H_2O)_3Cu_4I_6$ [28], and 0D $(PET)_4Cu_4I_4$ [29]. In such structures, carriers rely on hopping mechanisms or quantum tunneling for transport, resulting in a substantial reduction in carrier mobility. In contrast, one-dimensional (1D) OMHs feature infinite chains of metal halide tetrahedra with shared corners or edges. This structure effectively mitigates the erosion of water molecules and other environmental factors, facilitates directional carrier transport [30,31], and enables precise tuning of optoelectronic properties by adjusting the chain length and

* Corresponding author.
E-mail address: jiangxiaomei@sdfmu.edu.cn (X. Jiang).

https://doi.org/10.1016/j.cjsc.2025.100767
Received 7 August 2025; Received in revised form 16 September 2025; Accepted 5 October 2025
Available online 11 October 2025

arrangement [32,33]. Furthermore, the anisotropic nature of 1D structures also suppresses ion migration, a critical factor for realizing high-performance radiation detectors [17]. Despite these advantages, the application of 1D Cu(I)-based OMHs for direct X-ray detection remains largely unexplored. Synthesizing high-quality single crystals with excellent optoelectronic properties still poses a significant challenge.

In this work, a 1D Cu(I)-based OMH single crystal $(C_{12}H_{12}N)_3Cu_3I_6$ was grown via a facile solution cooling method. The crystal structure features $[CuI_4]$ tetrahedra interconnected through two shared iodide ions, forming infinite 1D chains that are separated by 4-benzylpyridine organic cations. This unique structure not only provides a robust framework for efficient directional charge transport but also ensures excellent structural stability. Notably, the centimeter-scale single crystal demonstrates superior X-ray detection performance, including high sensitivity, a prominent on-off ratio, and an ultra-low detection limit under 40 kV X-ray irradiation. Moreover, the device exhibits a significantly enhanced sensitivity at higher bias voltages. More importantly, it presents exceptional operational stability with negligible performance degradation even after 600 s of continuous X-ray radiation under ambient conditions, showcasing the great potential of $(C_{12}H_{12}N)_3Cu_3I_6$ for high-performance X-ray detection applications.

2. Results and discussion

The high-quality centimeter-scale $(C_{12}H_{12}N)_3Cu_3I_6$ single crystal was grown from a concentrated HI acid solution containing 4-benzylpyridine and CuI at a stoichiometric molar ratio of 1:2 via a facile cooling growth method (Fig. 1(a) and Fig. S1). The crystal structure was determined using a single-crystal X-ray diffractometer (SCXRD). It crystallizes in the monoclinic crystal system with $P2_1/n$ space group with $a = 6.6180(3)$, $b = 25.1998(11)$, $c = 26.4843(14)$ Å, $\alpha = \gamma = 90°$, and $\beta = 96.387(2)°$. Detailed crystallographic information is provided in Table S1. As depicted in Fig. 1(b and c), the inorganic component of the crystal is composed of adjacent tetrahedral $[CuI_4]$ units which exhibit an I–Cu–I bond angle ranging from 98.768° to 118.042° and a Cu–I bond length changing from 2.6294 to 2.7521 Å. They share edges via two I^- ions and extend along the *a*-axis to form a 1D chain structure, with a Cu–I–Cu bond angle of 72.099° (Fig. S2). This inorganic framework is encapsulated by 4-benzylpyridine organic cations, thereby enhancing the structural stability against the detrimental effects of moisture and oxygen [31]. To further evaluate its moisture stability, the water contact angle of $(C_{12}H_{12}N)_3Cu_3I_6$ single crystal was measured under ambient conditions. As shown in Fig. 1(d), the crystal exhibits a water contact angle of 65.829°, indicating better hydrophobic stability than many reported MHPs (Table S2) and thus confirming the favorable surface properties of the crystal [34]. Thermogravimetric analysis (TGA) was conducted in the temperature range from 25 to 900 °C at a heating rate of 5 °C min^{-1} to assess its thermal stability. Fig. 2(a) reveals that $(C_{12}H_{12}N)_3Cu_3I_6$ undergoes negligible weight loss up to 254.5 °C, superior to many previously reported OMHs (Table S3). Notably, it retains over 60% of its initial weight even at 600 °C, showcasing its excellent thermal stability.

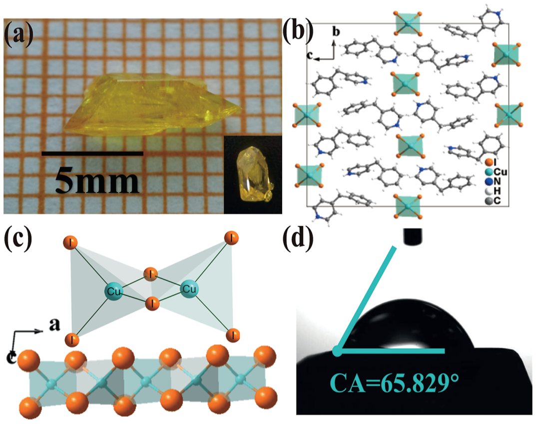

Fig. 1. (a) Photograph of $(C_{12}H_{12}N)_3Cu_3I_6$ single crystal. (b) Schematic illustration of the crystal structure viewed along the *a*-axis and (c) inorganic moiety for $(C_{12}H_{12}N)_3Cu_3I_6$. (d) Water contact angle test under ambient conditions.

The phase and purity of the single crystal were verified through powder X-ray diffraction (PXRD) measurements. Fig. 2(b) shows that the PXRD pattern of $(C_{12}H_{12}N)_3Cu_3I_6$ is highly consistent with the simulated data from SCXRD results, confirming the successful synthesis of high-purity material. To detect organic molecules within the crystal, Fourier transform infrared (FTIR) spectroscopy was performed. The spectrum exhibited characteristic peaks, such as an unsaturated C–H stretching vibration peak at 3070 cm^{-1} and a C=C vibration peak at 1498.5 cm^{-1}, which indicate the presence of aromatic compounds. Additionally, there is a N–H stretching vibration peak at 3226.9 cm^{-1} and a corresponding bending vibration peak at 1633.2 cm^{-1}, along with a stretching vibration peak at 1190.2 cm^{-1} and a C–H out-of-plane bending vibration peak at 738.6 cm^{-1} (Fig. 2(c)), thus proving the presence of 4-benzylpyridine in the crystal. Moreover, X-ray photoelectron spectroscopy (XPS) provided further evidence for the presence of carbon (C), nitrogen (N), copper (Cu), and iodine (I) elements in the crystal. As illustrated in Fig. 2(d), peaks at 618.75 and 630.27 eV correspond to I $3d_{5/2}$ and I $3d_{3/2}$, while those at 932.6 and 952.4 eV are assigned to Cu $2p_{3/2}$ and Cu $2p_{1/2}$, the characteristic peaks of Cu 2p, respectively. Furthermore, the high-resolution Cu 2p XPS spectrum revealed no presence of Cu^{2+} impurities (Fig. S3), proving that the Cu element exists solely as Cu^+ [35,36]. UV-vis absorption spectroscopy of $(C_{12}H_{12}N)_3Cu_3I_6$ was performed (Fig. 2(e)), and its indirect bandgap was calculated using the Tauc method (Fig. S4). The derived bandgap of 2.42 eV is consistent with the previously reported Cu-based OMHs, such as $(C_6H_9N_2)_2CuCl_4$ (2.45 eV) and $(C_6H_{18}N_2)_2Cu_2Cl_8$ (2.47 eV) [37]. The steady-state photoluminescence (PL) and excitation (PLE) spectra of $(C_{12}H_{12}N)_3Cu_3I_6$ reveal a yellow emission peak at 586 nm under optimal excitation with 450 nm blue light, with a Stokes shift of 136 nm (Fig. S5). To further validate the bandgap type, we performed systematic DFT calculations. The PBE functional predicts an indirect bandgap with a value of 0.528 eV, and this underestimation is a well-documented limitation of GGA-PBE. Specifically, it fails to fully capture the strong electron correlation in Cu–I clusters, leading to systematic bandgap underprediction, which is typically a 1–2 eV discrepancy for organic-inorganic hybrid halides [38–40]. Thus, the calculated bandgap value is not representative of the experimental value, but the indirect bandgap type is reliable, as confirmed by the distinct k-point positions of the valence band maximum (VBM at the H point) and the conduction band minimum (CBM at the E point), as shown in Fig. S6.

To evaluate its potential for X-ray detection, the absorption coefficient of $(C_{12}H_{12}N)_3Cu_3I_6$ was compared with that of several typical X-ray detector semiconductors using the XCOM database. Fig. 2(f) presents the X-ray absorption spectra across the photon energy range of 1–1000 keV. Notably, $(C_{12}H_{12}N)_3Cu_3I_6$ exhibits a similar linear absorption coefficient to some conventional X-ray detection semiconductors. Fig. 2(g) compares the corresponding attenuation efficiency as a function of thickness at 40 keV. A 1 mm-thick $(C_{12}H_{12}N)_3Cu_3I_6$ can achieve an X-ray absorption rate of up to 93.4%, which significantly outperforms Si (15.1%) and diamond (7%). To further demonstrate its direct X-ray detection performance, we fabricated a lateral-structured X-ray detector with the configuration Au (80 nm)/$(C_{12}H_{12}N)_3Cu_3I_6$ single crystal/Au (80 nm) (Fig. 2(h)). For direct X-ray detectors, shorter response time can reduce patient examination duration and consequently lower the absorbed radiation dose. Response time is defined as the duration from 10% to 90% of the saturated photocurrent (rise time) and from 90% to 10% (fall time) [22,41–44]. As shown in Fig. 2(i), the detector exhibits rapid response time of 20.08 ms (rise time) and 40.01 ms (fall time) under 200 V bias. Beyond response time, sensitivity (S) is another key metric for evaluating X-ray detector performance.

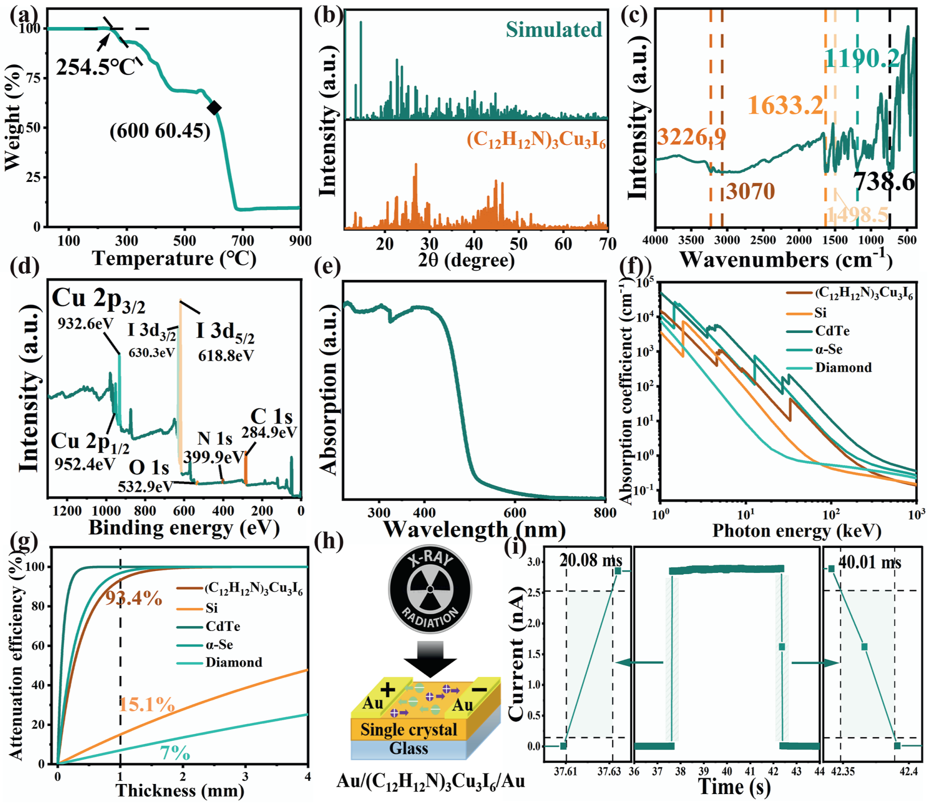

Fig. 2. (a) TG curve, (b) experimental and simulated PXRD patterns of $(C_{12}H_{12}N)_3Cu_3I_6$. (c) FTIR spectra and (d) XPS spectra of $(C_{12}H_{12}N)_3Cu_3I_6$. (e) UV-vis absorption spectrum of $(C_{12}H_{12}N)_3Cu_3I_6$. (f) X-ray absorption spectra of Si, α-Se, CdTe, $(C_{12}H_{12}N)_3Cu_3I_6$, and diamond. (g) Their X-ray attenuation efficiencies under 40 keV X-ray irradiation. (h) Schematic diagram of lateral-structured X-ray detector. (i) Transient X-ray response of the $(C_{12}H_{12}N)_3Cu_3I_6$-based detector.

Detectors with high sensitivity can improve the image quality while reducing patient radiation dose, thereby minimizing the risks of irradiation-induced cancer [10,45]. The sensitivity of the detector can be calculated via Eq. (1) [46]:

$$S = \frac{I_p - I_d}{D \times A} \tag{1}$$

where I_p is the photocurrent, I_d is the dark current, D is the X-ray dose rate, and A is the effective detection area. To calculate the sensitivity of the detector, its photocurrent responses were measured under different dose rates from 66.1 to 4123 $\mu Gy \cdot s^{-1}$ at varying bias voltages.

Fig. 3(a) and Fig. S7 demonstrate the variation in X-ray current response with dose rate for 40, 50, 70, 120 kV radiation at bias voltages ranging from 1 to 200 V, and with a constant bias voltage of 200 V, respectively. The corresponding dose rates for these measurements are given in Table S4. By comparison, the current responses of the detector are positively correlated with the applied bias voltage, X-ray tube voltage and the dose rate, consistent with the expected pattern [50]. More strikingly, under a bias voltage of 200 V, an active area of 0.0005 cm^2 and an X-ray tube voltage of 120 kV, the detector exhibits a dark current of 1.35 pA and a photocurrent of 2889.87 pA at a maximum dose rate of 4123 $\mu Gy \cdot s^{-1}$ (Fig. S8), with the highest on-off ratio of 2140 compared with that obtained under 40, 50, and 70 kV X-ray irradiation. This performance indicates enhanced charge collection efficiency, which can be attributed to the fact that high-energy X-rays possess stronger penetrating power and higher energy. The secondary electrons, such as photoelectrons and Compton electrons, generated through their interaction with the detector material carry higher energy, enabling them to excite more electron-hole pairs within the detector material [51, 52]. Consequently, this leads to an increased number of charge carriers being produced. Additionally, as shown in Fig. 3(b) and Fig. S9, the current density exhibits a perfect linear relationship with dose rate under different bias voltages and for 40, 50, 70, and 120 kV X-ray irradiation. The sensitivity of the detector was calculated under different bias voltages and dose rates. As illustrated in Fig. 3(c), the detector achieves a sensitivity of 265.72 $\mu C \cdot Gy^{-1} \cdot cm^{-2}$ under 40 kV radiation at 10 V bias. This performance surpasses the sensitivity of detectors exposed to 50, 70, and 120 kV radiation at the same bias voltage, exceeding the sensitivity of commercial α-Se detectors (20 $\mu C \cdot Gy^{-1} \cdot cm^{-2}$) by more than tenfold [22,53,54]. Furthermore, the sensitivity exhibits a linear growth trend with increasing bias voltage, achieving 1464.14 $\mu C \cdot Gy^{-1} \cdot cm^{-2}$ at 200 V bias. The limit of detection (LoD) is another crucial metric for assessing the performance of X-ray detectors. A low detection limit is capable of delivering high-quality imaging at significantly reduced radiation doses [22]. According to the International Union of Pure and Applied Chemistry (IUPAC), the LoD is defined as the dose rate at a signal-to-noise ratio (SNR) of 3. The SNR can be described by Eq. (2) [55]:

$$SNR = \frac{I_p - I_d}{\sqrt{\frac{1}{N}\sum_i^n \left(I_i - I_p\right)^2}} \tag{2}$$

where I_d is the average of measured dark currents, I_p is the average of measured photocurrents, and I_i is the measured photocurrent, respectively. By calculation, the LoD value of $(C_{12}H_{12}N)_3Cu_3I_6$-based device is 19.8 $nGy \cdot s^{-1}$ at 10 V bias, which is much lower than the clinical diagnostic requirements of 5.5 $\mu Gy \cdot s^{-1}$ (Fig. 3(d) and Fig. S10) [22]. It is worth noting that $(C_{12}H_{12}N)_3Cu_3I_6$ exhibits superior performance in sensitivity and detection limit compared to many recently reported MHPs, such as the sensitivity values of 148, 114.9, 242, 1106.44 $\mu C \cdot Gy^{-1} \cdot cm^{-2}$ and the LoD values of 241, 3483, 430, 130.1 $nGy \cdot s^{-1}$ for $(BA)_2PbI_4$ [47], $(3PA)PbI_4$ [48], $(BDA)PbI_4$ [49] and $(2FEA)_2CuCl_4$ [45] at 10 V bias, respectively (Fig. 3(e)) [45,47–49].

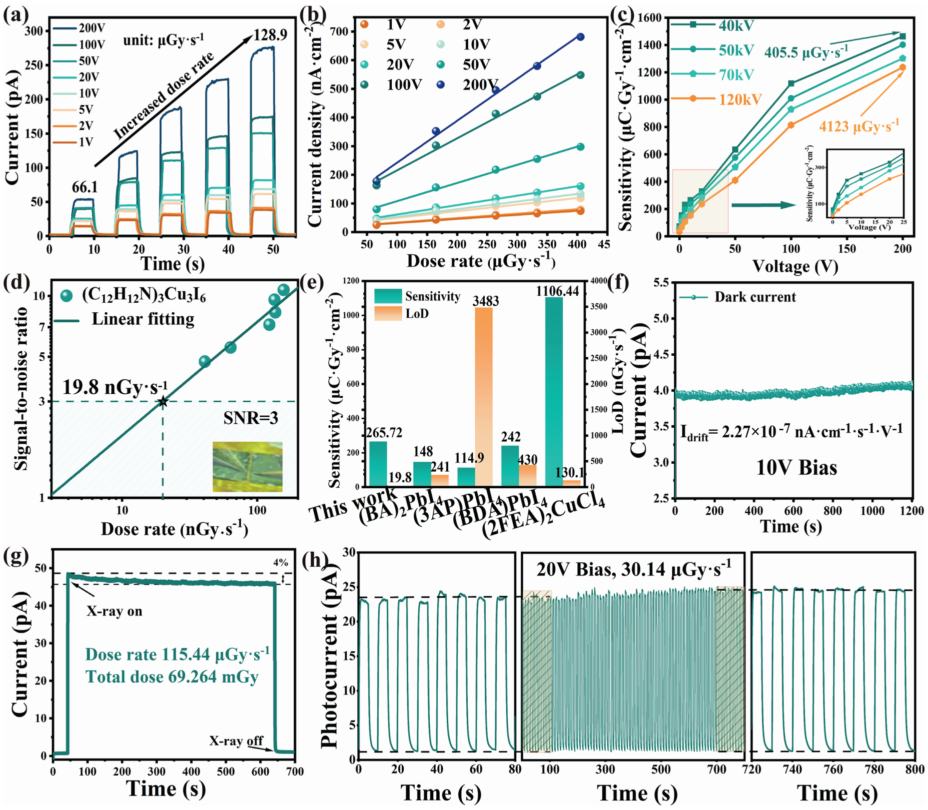

Fig. 3. (a) X-ray response current under varying dose rates and different bias voltages. (b) Dose rate-dependent current density under 40 kV X-ray irradiation at varying bias voltages. (c) Detector sensitivity under 1–200 V bias and 40, 50, 70, 120 kV X-ray irradiation. (d) Signal-to-noise ratio at 10 V bias under 40 kV X-ray exposure of the detector. (e) Comparison of properties of several MHPs at 10 V bias [45,47–49]. (f) Dark current drift measurement and (g) X-ray current stability at 10 V bias. (h) X-ray response current stability to on-off 40 kV X-ray at 20 V bias.

Moreover, $(C_{12}H_{12}N)_3Cu_3I_6$ exhibits a low dark current drift (I_{drift}), which effectively reduces device noise, optimizes SNR, and thereby lowers detection limit. The dark current was recorded for 1200 s under 10 V bias (Fig. 3(f)), after which I_{drift} was calculated according to the following Eq. (3) [45]:

$$I_{\mathrm{drift}} = \frac{I_t - I_0}{EAt} \tag{3}$$

where I_0 is the initial current, I_t is the current at time t, E is the electric field, A is the device active area, and t is the time. The I_{drift} value is calculated to be 2.27×10^{-7} nA cm^{-1} s^{-1} V^{-1}, which is lower than that of many reported MHPs (Table S5), demonstrating low ion migration of the detector. Additionally, when the device is continuously irradiated with 70 kV X-rays at a dose rate of 115.44 μGy·s^{-1} under 10 V bias, it can be observed from Fig. 3(g) that the current response decreases by only approximately 4% relative to its initial value after about 600 s of irradiation. Cycling irradiation tests under varying bias voltages further verified the operational stability of the device. Specifically, the detector was subjected to 80 times repeated cycles of 40 kV X-ray irradiation at a dose rate of 30.14 μGy·s^{-1} under 20 V and 200 V bias to test its response stability under on-off X-rays (Fig. 3(h) and Fig. S11). There were no significant fluctuations in neither photocurrent nor dark current, demonstrating the detector with excellent cycling stability. Notably, defect density is a crucial parameter closely related to charge carrier transport and device stability, as high defect density tends to enhance carrier scattering and ion migration, which in turn leads to performance fluctuations over time. To evaluate this key parameter, we fabricated a device with the vertical structure Ag/$(C_{12}H_{12}N)_3Cu_3I_6$/Ag. Its electrode area and thickness were measured to be 0.126 cm^2 and 0.22 cm, respectively. This configuration corresponds to a parallel-plate capacitor with $(C_{12}H_{12}N)_3Cu_3I_6$ as the dielectric. Subsequently, its capacitance was measured using an LCR digital bridge (TH2838H), and the relative permittivity of $(C_{12}H_{12}N)_3Cu_3I_6$ was calculated via the following Eq. (4):

$$C = \frac{\varepsilon\varepsilon_0 S}{D} \tag{4}$$

where C represents capacitance, S denotes electrode area, ε_0 is the vacuum permittivity, ε is the relative permittivity, and D indicates the thickness of the material. Calculations yield a relative permittivity value of 9.06. The defect density can be calculated via Eq. (5):

$$V_{\mathrm{TFL}} = \frac{e n_{\mathrm{trap}} L^2}{\varepsilon_0 \varepsilon} \tag{5}$$

Here, e represents the elementary charge, n_{trap} denotes the defect density, L is the sample thickness, and V_{TFL} is the turn-on voltage under defect state filling, which can be estimated from the space-charge-limited current curve. The space-charge-limited current (SCLC) method refers to the specific relationship between current and voltage when a device operates within the space-charge-limited current region. By measuring the current at different voltages and fitting the corresponding theoretical curve, V_{TFL} can be determined. We employed a high-precision semiconductor parameter tester to measure the current-voltage (I–V) characteristics of the device under various bias conditions. By fitting the measured I–V curves to the SCLC theoretical model, we determined the V_{TFL} of the material to be 17.4 V (Fig. S12). Substituting this value into Eq. (5) yields n_{trap} as 1.8×10^{11} cm^{-3}. In addition to defect density, the carrier mobility-lifetime product ($\mu\tau$) is another critical parameter governing charge collection efficiency, which is a key metric for direct X-ray detectors. Its magnitude is typically obtained by fitting the modified Hecht equation, with the specific Eq. (6) as follows:

$$I = \frac{I_0 \mu\tau V}{d^2}\left[1 - \exp\left(\frac{-d^2}{\mu\tau V}\right)\right] \tag{6}$$

In the equation, I_0 represents the saturation photocurrent, d denotes the period thickness, and V represents the applied bias voltage. By measuring the photoconductivity under 1 sun illumination (AM 1.5 G,

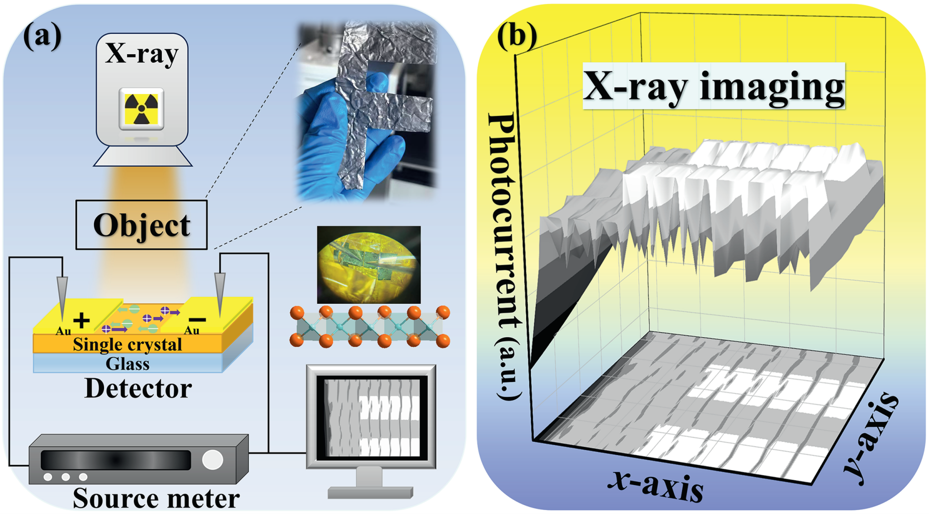

Fig. 4. (a) Schematic illustration of our home-built X-ray imaging system. (b) 3D projection image acquired by $(C_{12}H_{12}N)_3Cu_3I_6$-based detector for a 0.1 mm-thick lead sheet cut into an "F" shape.

100 mW/cm^2) with different bias voltages applied to the device, and fitting the resulting curves, we obtained a $\mu\tau$ value of 1.26×10^{-4} cm^2/V for the material (Fig. S13). These data even outperform some previously reported lead-based OMHs materials, such as 1.73×10^{-5} cm^2/V of $(BDA)(MA)_2Pb_3Br_{10}$ [13] and 1.2×10^{-5} cm^2/V $(PEA)_2PbI_4$ [56].

The above properties demonstrate the potential of $(C_{12}H_{12}N)_3Cu_3I_6$ in X-ray detection applications, thus prompting corresponding imaging tests. Fig. 4(a) illustrates our home-built X-ray imaging system. A 0.1 mm-thick lead sheet was cut into an "F" shape as an imaging target. The detector was positioned beneath the target, and raw data were acquired by moving the lead sheet using an (x, y) translation stage. After data processing, a 3D projection image of the "F"-shaped target can be reconstructed, as shown in Fig. 4(b), clearly validating the direct imaging capability of the $(C_{12}H_{12}N)_3Cu_3I_6$ detector.

3. Conclusion

In summary, a non-toxic 1D Cu(I)-based OMH $(C_{12}H_{12}N)_3Cu_3I_6$ was grown and characterized, demonstrating excellent X-ray detection properties. The lateral-structured detector with configuration Au/$(C_{12}H_{12}N)_3Cu_3I_6$ single crystal/Au exhibits a maximum sensitivity of 1464.14 μC·Gy^{-1}·cm^{-2} at 200 V bias, a low dark current drift of 2.27×10^{-7} nA·cm^{-1} s^{-1}·V^{-1}, and a low detection limit of 19.8 nGy·s^{-1} under 40 kV irradiation. A preliminary prototype device successfully reconstructed a clear projection image of a 0.1 mm-thick lead sheet using a home-built X-ray imaging system, demonstrating the feasibility of this material for practical imaging applications. This work not only enriches the application domain of Cu(I)-based OMHs as X-ray detection semiconductors, but also paves the way for the rational design of non-toxic, high-performance radiation detection materials in the field of optoelectronic devices.

CRediT authorship contribution statement

Pan Gao: Writing – review & editing, Writing – original draft, Software, Methodology, Investigation, Formal analysis, Data curation. **Qingzheng Kong:** Software, Formal analysis, Data curation. **Ying Sun:** Writing – original draft, Validation, Methodology, Investigation, Formal analysis, Data curation. **Qian Ma:** Data curation, Formal analysis, Methodology, Software, Validation. **Qi Wang:** Validation, Data curation. **Zeyu Guo:** Validation, Data curation. **Ledi Li:** Validation, Data curation. **Bingbing Li:** Methodology, Investigation. **Jingwei Xu:** Validation, Data curation. **Xiaomei Jiang:** Writing – review & editing, Supervision, Resources, Project administration, Investigation, Funding acquisition, Formal analysis, Conceptualization. **Zhaolai Chen:** Writing – review & editing, Supervision, Conceptualization.

Declaration of competing interest

The authors declare no competing interests.

Acknowledgements

This work was financially supported by the National Natural Science Foundation of China (62305195), the Shandong Provincial Natural Science Foundation (ZR2022QF036 and ZR2025MS1001), and Shandong Provincial Youth Innovation Technology Program (2024KJN010).

Appendix A. Supplementary data

Supplementary data to this article can be found online at https://doi.org/10.1016/j.cjsc.2025.100767.

References

[1] M. Chen, X. Dong, D. Chu, B. Jia, X. Zhang, Z. Zhao, J. Hao, Y. Zhang, J. Feng, X. Ren, Y. Liang, R. Shi, A. Najar, Y. Liu, S.F. Liu, Interlayer-spacing engineering of lead-free perovskite single crystal for high-performance X-ray imaging, Adv. Mater. 35 (2023) 2211977, https://doi.org/10.1002/adma.202211977.

[2] A. Jana, S. Cho, S.A. Patil, A. Meena, Y. Jo, V.G. Sree, Y. Park, H. Kim, H. Im, R. A. Taylor, Perovskite: scintillators, direct detectors, and X-ray imagers, Mater. Today 55 (2022) 110–136, https://doi.org/10.1016/j.mattod.2022.04.009.

[3] G. Zheng, H. Wu, S. He, H. Li, Z. Dong, T. Jin, J. Pang, R. Masrour, Z. Zheng, G. Niu, L. Xu, J. Tang, High-performing direct X-ray detection made of one-dimensional perovskite-like $(TMHD)SbBr_5$ single crystal with anisotropic response, Small 21 (2025) 2408720, https://doi.org/10.1002/smll.202408720.

[4] J. Fan, W. Li, Q. Zhou, G. Yang, P. Tang, J. He, L. Ma, J. Zhang, J. Xiao, Z. Yan, A. Li, X. Han, Metal halide perovskites for direct X-ray detection in medical imaging: to higher performance, Adv. Funct. Mater. 35 (2025) 2401017, https://doi.org/10.1002/adfm.202401017.

[5] X. Xu, W. Qian, S. Xiao, J. Wang, S. Zheng, S. Yang, Halide perovskites: a dark horse for direct X-ray imaging, EcoMat 2 (2020) e12064, https://doi.org/10.1002/eom2.12064.

[6] L. Sun, W. Li, W. Zhu, Z. Chen, Single-crystal perovskite detectors: development and perspectives, J. Mater. Chem. C 8 (2020) 11664–11674, https://doi.org/10.1039/d0tc02944k.

[7] Q. Wei, X. Fan, P. Xiang, L. Qin, W. Liu, T. Shi, H. Yin, P. Cai, Y. Tong, G. Tang, Z. Liu, P.K. Chu, H. Shi, Y. Liu, X.F. Yu, $Cs_3Cu_2I_5$ single crystal for efficient direct X-ray detection, Adv. Opt. Mater. 11 (2023) 2300247, https://doi.org/10.1002/adom.202300247.

[8] H. Li, J. Song, W. Pan, D. Xu, W.A. Zhu, H. Wei, B. Yang, Sensitive and stable 2D perovskite single-crystal X-ray detectors enabled by a supramolecular anchor, Adv. Mater. 32 (2020) 2003790, https://doi.org/10.1002/adma.202003790.

[9] Z. Li, F. Zhou, H. Yao, Z. Ci, Z. Yang, Z. Jin, Halide perovskites for high-performance X-ray detector, Mater. Today 48 (2021) 155–175, https://doi.org/10.1016/j.mattod.2021.01.028.
[10] B.M. Saidzhonov, K.E. Yorov, P. Yuan, S. Nematulloev, A.A. Karluk, T. Ahmad, O. F. Mohammed, O.M. Bakr, M. Bayindir, Multimaterial fibers with nanoemitters enable conformal X-ray imaging with 3D printed and woven scintillators, ACS Mater. Lett. 6 (2024) 1779–1789, https://doi.org/10.1021/acsmaterialslett.3c01359.
[11] A. Feng, X. Jiang, X. Zhang, X. Zheng, W. Zheng, O.F. Mohammed, Z. Chen, O. M. Bakr, Shape control of metal halide perovskite single crystals: from bulk to nanoscale, Chem. Mater. 32 (2020) 7602–7617, https://doi.org/10.1021/acs.chemmater.0c02269.
[12] H. Zhang, F. Wang, Y. Lu, Q. Sun, Y. Xu, B.-B. Zhang, W. Jie, M.G. Kanatzidis, High-sensitivity X-ray detectors based on solution-grown caesium lead bromide single crystals, J. Mater. Chem. C 8 (2020) 1248–1256, https://doi.org/10.1039/c9tc05490a.
[13] S. Wang, F. Wang, X. Xu, N. Zhang, R. Zhang, L. Lv, X. Jiang, X. Huang, S. Wu, Y. Ding, Methylammonium-based quasi-two-dimensional perovskite single crystals for highly sensitive X-ray detection and imaging, ACS Appl. Mater. Interfaces 15 (2023) 58566–58572, https://doi.org/10.1021/acsami.3c12866.
[14] Y. Huang, L. Qiao, Y. Jiang, T. He, R. Long, F. Yang, L. Wang, X. Lei, M. Yuan, J. Chen, A-site cation engineering for highly efficient $MAPbI_3$ single-crystal X-ray detector, Angew Chem. Int. Ed. 58 (2019) 17834–17842, https://doi.org/10.1002/anie.201911281.
[15] Z.P. Zhang, Z.J. Zhang, W. Zheng, K. Wang, H. Chen, S. Deng, F. Huang, J. Chen, Sensitive and fast direct conversion X-ray detectors based on single-crystalline HgI_2 photoconductor and ZnO nanowire vacuum diode, Adv. Mater. Technol. 5 (2020) 1901108, https://doi.org/10.1002/admt.201901108.
[16] X. Liu, J. Ren, Y.-A. Chen, X. Geng, D. Xie, T.-L. Ren, Recent progress in single crystal perovskite X-ray detectors, Sci. China Inf. Sci. 67 (2024) 131401, https://doi.org/10.1007/s11432-023-3856-4.
[17] Y. He, I. Hadar, M.C. De Siena, V.V. Klepov, L. Pan, D.Y. Chung, M.G. Kanatzidis, Sensitivity and detection limit of spectroscopic-grade perovskite $CsPbBr_3$ crystal for hard X-ray detection, Adv. Funct. Mater. 32 (2022) 2112925, https://doi.org/10.1002/adfm.202112925.
[18] D. Gao, R. Li, X. Chen, C. Chen, C. Wang, B. Zhang, M. Li, X. Shang, X. Yu, S. Gong, T. Pauporte, H. Yang, L. Ding, J. Tang, J. Chen, Managing interfacial defects and carriers by synergistic modulation of functional groups and spatial conformation for high-performance perovskite photovoltaics based on vacuum flash method, Adv. Mater. 35 (2023) 2301028, https://doi.org/10.1002/adma.202301028.
[19] C. Li, C. Chen, Single-crystal perovskite for solar cell applications, Small 20 (2024) 2402759, https://doi.org/10.1002/smll.202402759.
[20] H. Li, Y. He, W. Li, T. Lu, M. Tan, W. Wei, B. Yang, H. Wei, Perovskite dimensional evolution through cations engineering to tailor the detection limit in hard X-ray response, Small 18 (2022) 2203884, https://doi.org/10.1002/smll.202203884.
[21] X. Li, G. Zhang, Y. Hua, X. Sun, J. Liu, H. Liu, Z. Yue, Z. Zhai, H. Xia, X. Tao, Two-dimensional lead-free perovskite $Cs_3Bi_2I_{8.3}Br_{0.7}$ single crystals with anisotropic ion migration and hard X-ray responses, J. Mater. Chem. C 12 (2024) 10613–10620, https://doi.org/10.1039/d4tc01131g.
[22] X. Geng, Y.A. Chen, Y.Y. Li, J. Ren, G.H. Dun, K. Qin, Z. Lin, J. Peng, H. Tian, Y. Yang, D. Xie, T.L. Ren, Lead-free halide perovskites for direct X-ray detectors, Adv. Sci. 10 (2023) 2300256, https://doi.org/10.1002/advs.202300256.
[23] B. Yang, L. Yin, G. Niu, J.H. Yuan, K.H. Xue, Z. Tan, X.S. Miao, M. Niu, X. Du, H. Song, E. Lifshitz, J. Tang, Lead-free halide Rb_2CuBr_3 as sensitive X-ray scintillator, Adv. Mater. 31 (2019) 1904711, https://doi.org/10.1002/adma.201904711.
[24] W. Gao, G. Niu, L. Yin, B. Yang, J.-H. Yuan, D. Zhang, K.-H. Xue, X. Miao, Q. Hu, X. Du, J. Tang, One-dimensional all-inorganic K_2CuBr_3 with violet emission as efficient X-ray scintillators, ACS Appl. Electron. Mater. 2 (2020) 2242–2249, https://doi.org/10.1021/acsaelm.0c00414.
[25] C. Ma, H. Li, M. Chen, Y. Liu, K. Zhao, S. Liu, Water-resistant lead-free perovskitoid single crystal for efficient X-ray detection, Adv. Funct. Mater. 32 (2022) 2202160, https://doi.org/10.1002/adfm.202202160.
[26] S. Dutta, D. Vishnu, S. K, S. Som, R. Chaurasiya, D.K. Patel, K. Moovendaran, C.-C. Lin, C.-W. Chen, R. Sankar, Segmented highly reversible thermochromic layered perovskite $[(CH_2)_2(NH_3)_2]CuCl_4$ crystal coupled with an inverse magnetocaloric effect, ACS Appl. Electron. Mater. 4 (2022) 521–530, https://doi.org/10.1021/acsaelm.1c01108.
[27] S. Cao, J.A. Lai, Y. Wang, K. An, T. Jiang, M. Wu, P. He, P. Feng, X. Tang, Vacuum-filtration fabrication of copper-based halide scintillation screen for high-resolution X-ray imaging, J. Lumin. 277 (2025) 120877, https://doi.org/10.1016/j.jlumin.2024.120877.
[28] J. Huang, B. Su, E. Song, M.S. Molokeev, Z. Xia, Ultra-broad-band-excitable Cu(I)-Based organometallic halide with near-unity emission for light-emitting diode applications, Chem. Mater. 33 (2021) 4382–4389, https://doi.org/10.1021/acs.chemmater.1c00085.
[29] L. Wang, H. Sun, C. Sun, D. Xu, J. Tao, T. Wei, Z.H. Zhang, Y. Zhang, Z. Wang, W. Bi, Lead-free, stable orange-red-emitting hybrid copper based organic-inorganic compounds, Dalton Trans. 50 (2021) 2766–2773, https://doi.org/10.1039/d0dt04413j.
[30] F. Wang, K. Zhou, C. Zhou, X. Liang, T. Wang, Y. Sun, Y. Li, Q. Li, X. Zhou, G. Yang, D. Duan, J. Zhu, Q. Zhu, H. Lin, Y. Shi, C. Yang, G. Xing, H. Hu, Ionic liquid-induced 1D perovskite: exploring 1D perovskite structure to 1D/3D heterojunction-based photovoltaics, Adv. Energy Mater. 14 (2024) 2400021, https://doi.org/10.1002/aenm.202400021.
[31] Y. Chen, B. Liu, Q. Zhou, D. Ma, X. Han, D. He, S. Chen, Y. Li, S. Lu, Z.-X. Xu, C. Chen, H. Yu, J. Chen, Critical role of 1D materials in realizing efficient and stable perovskite solar cells, J. Mater. Chem. A 11 (2023) 18592–18604, https://doi.org/10.1039/d3ta03174h.
[32] D. Duan, C. Ge, M.Z. Rahaman, C.-H. Lin, Y. Shi, H. Lin, H. Hu, T. Wu, Recent progress with one-dimensional metal halide perovskites: from rational synthesis to optoelectronic applications, NPG Asia Mater. 15 (2023) 8, https://doi.org/10.1038/s41427-023-00465-0.
[33] A. Mei, X. Peng, X. Li, G. Zhang, S. Lin, N. Fu, Anions regulation of 1D perovskite intrusion-behavior for efficient and stable perovskite solar cells, ACS Appl. Mater. Interfaces 16 (2024) 31209–31217, https://doi.org/10.1021/acsami.4c06087.
[34] X. Wu, J. Deng, T. Yang, L. Fu, J. Xu, Small molecule induced interfacial defect healing to construct inverted perovskite solar cells with high fill factor and stability, J. Colloid Interface Sci. 678 (2025) 776–784, https://doi.org/10.1016/j.jcis.2024.08.186.
[35] Z. Zang, X. Yang, X. Yang, Z. Liu, Q. Qian, S.M.H. Qaid, A.S. Aldwayyan, B. Wang, S. Zhao, Excitation-wavelength-induced dual-band fluorescence of copper halides for multi-mode encryption and anti-counterfeiting applications, Adv. Opt. Mater. 13 (2025) 2403177, https://doi.org/10.1002/adom.202403177.
[36] B. Wang, X. Yang, R. Li, S.M.H. Qaid, W. Cai, H. Xiao, Z. Zang, One-dimensional $CsCu_2I_3$ single-crystal X-ray detectors, ACS Energy Lett. 8 (2023) 4406–4413, https://doi.org/10.1021/acsenergylett.3c01581.
[37] X. Wei, S. Chen, G. Zheng, Q. Zhao, S. Mo, J. Wang, D. Yao, N. Tian, F. Long, Synthesis, crystal structure, thermal stability, and photovoltaic properties of organic-inorganic hybridized copper-based perovskite single crystals modulated by organics, J. Mol. Struct. 1304 (2024) 137634, https://doi.org/10.1016/j.molstruc.2024.137634.
[38] Y. Zhu, X. Yang, L. Xu, G. Jia, J. Du, Hollow microscale and nanoscale structures as anode materials for lithium-ion batteries, Chem. Mater. 34 (2022) 9803–9822, https://doi.org/10.1021/acs.chemmater.2c02870.
[39] D. Huang, C. Cao, H. Cheng, D. Wang, W. Yang, R. Xie, Zero-dimensional organic-inorganic hybrid cuprous halide of $(C_{20}H_{20}OP)CuCl_2$ with high anti-water stability, Mater. Today Chem. 37 (2024) 102010, https://doi.org/10.1016/j.mtchem.2024.102010.
[40] T. Li, B. Tang, J. Jin, K. Han, H. Zhang, H. Zhao, X. Zhang, M. Molokeev, Y. Wang, Z. Xia, B. Lei, Single organic cation engineering Cu(I)-based ionic and coordinate type halides as high-efficiency hydrogel scintillator, Adv. Mater. 37 (2025) e09478, https://doi.org/10.1002/adma.202509478.
[41] T.C. Wang, S.Y. Yao, S.P. Yan, J. Yu, Z.Y. Deng, A.N. Yakovlev, B. Meng, J.B. Qiu, X.H. Xu, High thermal stability of copper-based perovskite scintillators for high-temperature X-ray detection, ACS Appl. Mater. Interfaces 15 (2023) 23421–23428, https://doi.org/10.1021/acsami.3c02041.
[42] C.-X. Qian, S.-S. Lu, D. Chu, Y. Liu, H.-J. Feng, Cu ion implantation induced efficient interface carrier extraction for ultra-sensitive $DMAPbI_3$ single crystal perovskite X-ray detector, Chem. Eng. J. 474 (2023) 145535, https://doi.org/10.1016/j.cej.2023.145535.
[43] L. Li, H. Chen, Z. Fang, X. Meng, C. Zuo, M. Lv, Y. Tian, Y. Fang, Z. Xiao, C. Shan, Z. Xiao, Z. Jin, G. Shen, L. Shen, L. Ding, An electrically modulated single-color/dual-color imaging photodetector, Adv. Mater. 32 (2020) 1907257, https://doi.org/10.1002/adma.201907257.
[44] W. Pan, B. Yang, G. Niu, K.H. Xue, X. Du, L. Yin, M. Zhang, H. Wu, X.S. Miao, J. Tang, Hot-pressed $CsPbBr_3$ quasi-monocrystalline film for sensitive direct X-ray detection, Adv. Mater. 31 (2019) 1904405, https://doi.org/10.1002/adma.201904405.
[45] Y. Lv, X. Lin, F. Wu, Z. Yue, F. Zhang, X. Li, Q. Wei, K. Li, Q. Wang, J. Luo, X. Liu, Inch-sized single crystals of radiation-sensitive copper-based hybrid perovskites for direct X-ray detection, Inorg. Chem. Front. (2025) 2691–2697, https://doi.org/10.1039/d5qi00263j.
[46] Y. Wu, J. Feng, Z. Yang, Y. Liu, S.F. Liu, Halide perovskite: a promising candidate for next-generation X-ray detectors, Adv. Sci. 10 (2022) 2205536, https://doi.org/10.1002/advs.202205536.
[47] Yukta J. Ghosh, M.A. Afroz, S. Alghamdi, P.J. Sellin, S. Satapathi, Efficient and highly stable X-ray detection and imaging using 2D $(BA)_2PbI_4$ perovskite single crystals, ACS Photonics 9 (2022) 3529–3539, https://doi.org/10.1021/acsphotonics.2c00776.
[48] C. Ma, L. Gao, Z. Xu, X. Li, X. Song, Y. Liu, T. Yang, H. Li, Y. Du, G. Zhao, X. Liu, M. G. Kanatzidis, S.F. Liu, K. Zhao, Centimeter-sized 2D perovskitoid single crystals for efficient X-ray photoresponsivity, Chem. Mater. 34 (2022) 1699–1709, https://doi.org/10.1021/acs.chemmater.1c03832.
[49] Y. Shen, Y. Liu, H. Ye, Y. Zheng, Q. Wei, Y. Xia, Y. Chen, K. Zhao, W. Huang, S. Liu, Centimeter-sized single crystal of two-dimensional halide perovskites incorporating straight-chain symmetric diammonium ion for X-ray detection, Angew. Chem. Int. Ed. 59 (2020) 14896–14902, https://doi.org/10.1002/anie.202004160.
[50] J. Li, T. Zhu, H. Ye, Q. Guan, S. You, R. Li, Y. Geng, J. Luo, Achieving high operating-temperature self-powered X-ray detection in multilayered hybrid perovskites through arylamine intercalation, Small 20 (2024) 2401545, https://doi.org/10.1002/smll.202401545.
[51] S. Tao, C. He, X. Hao, C. Kuang, X. Liu, Principles of different X-ray phase-contrast imaging: a review, Appl. Sci. 11 (2021) 2971, https://doi.org/10.3390/app11072971.
[52] P. Bharathan, Investigation of properties of As_xSe_{1-x} thin films for direct conversion, J. Electron. Mater. 44 (2015) 2725–2735, https://doi.org/10.1007/s11664-015-3758-9.
[53] H. Huang, S. Abbaszadeh, Recent developments of amorphous selenium-based X-ray detectors: a review, IEEE Sens. J. 20 (2020) 1694–1704, https://doi.org/10.1109/jsen.2019.2950319.
[54] X. Xu, Y. Wu, Y. Zhang, X. Li, F. Wang, X. Jiang, S. Wu, S. Wang, Two-dimensional perovskite single crystals for high-performance X-ray imaging and exploring MeV

X-ray detection, Energy Environ. Mater. 7 (2023) e12487, https://doi.org/10.1002/eem2.12487.

[55] X. Li, G. Zhang, Y. Hua, F. Cui, X. Sun, J. Liu, H. Liu, Y. Bi, Z. Yue, Z. Zhai, H. Xia, X. Tao, Dimensional and optoelectronic tuning of lead-free perovskite $Cs_3Bi_2I_{9-n}Br_n$ single crystals for enhanced hard X-ray detection, Angew. Chem. Int. Ed. 62 (2023) e202315817, https://doi.org/10.1002/anie.202315817.

[56] Y. Liu, Z. Xu, Z. Yang, Y. Zhang, J. Cui, Y. He, H. Ye, K. Zhao, H. Sun, R. Lu, M. Liu, M.G. Kanatzidis, S. Liu, Inch-size 0D-structured lead-free perovskite single crystals for highly sensitive stable X-ray imaging, Matter 3 (2020) 180–196, https://doi.org/10.1016/j.matt.2020.04.017.